

Enhanced optical nonlinearities in epitaxial quantum dots lasers on silicon for future photonic integrated systems

Jianan Duan,^{1,2,*} Weng W. Chow,³ Bozhang Dong,¹ Heming Huang,¹ Songtao Liu,⁴ Justin C. Norman,⁴ John E. Bowers,⁴ and Frédéric Grillot^{1,5}

¹ LTCI, Télécom Paris, Institut Polytechnique de Paris, 91120, Palaiseau, France

² State Key Laboratory on Tunable Laser Technology, School of Electronic and Information Engineering, Harbin Institute of Technology, Shenzhen, 518055, China

³ Sandia National Laboratories, Albuquerque, NM 87185, USA

⁴ Department of Electrical and Computer Engineering, Materials Department, University of California Santa Barbara, Santa Barbara, CA 93106, USA

⁵ Center for High Technology Materials, University of New-Mexico, Albuquerque, NM 87106, USA

Abstract. Four-wave mixing (FWM) is an important nonlinear optical phenomenon that underlines many of the discoveries and device applications since the laser was invented. Examples include parametric amplification, mode-locked pulses and frequency combs, and in the quantum optics regime, entangled-photon generation, squeezed-state production and optical transduction from the visible to infrared wavelengths. For quantum dot systems, the basic understanding of FWM is limited by the conventional investigation method, which concentrates on the FWM susceptibility measured with optical amplifiers. This paper addresses this weakness by performing laser experiments to account for all optical nonlinearities contributing to the FWM signal. Meanwhile, we gain valuable insight into the intricate interplay among optical nonlinearities. Using quantum dot lasers directly grown on silicon, we achieved FWM conversion efficiency sufficient to demonstrate self-mode-locking in a single-section laser diode, with sub-ps mode-locked pulse duration and kHz frequency-comb linewidth. A comparison with first-principles based multimode laser theory indicates measured FWM conversion efficiencies that are close to the theoretical limit. An advantage over earlier studies and crucial to confidence in the results are the quality and reproducibility of state-of-the-art quantum dot lasers. They make possible the detailed study of conversion efficiency over a broad parameter space, and the identification of the importance of p-doping. Systematic improvement based on our understanding of underlying physics will lead to transform limited performance and effective compensation of intrinsic and extrinsic effects, such as linewidth enhancement and background dispersion. The integration of FWM with lasing impacts numerous optoelectronic components used in telecom and datacom.

Keywords: quantum dot laser, four-wave mixing, optical nonlinearities, self-mode-locking.

*Jianan Duan, E-mail: jianan.duan@hotmail.com

1 Introduction

Photonic integrated circuits (PICs) on silicon can significantly advance the level of component integration and performance necessary for taking both conventional and quantum information processing outside the laboratory¹. The advantages of silicon-based PICs are the availability of manufacturing approaches using modern nanofabrication techniques as well as the potential for miniaturization and integration of optoelectronic components with complementary functionalities². In this situation, quantum dot (QD) nanostructures are highly promising semiconductor atoms that can be integrated either monolithically or heterogeneously on a compact and scalable platform³⁻⁶. As a direct consequence of the size-confinement effect of the trapped electrons and holes, QD

based photonic devices have shown remarkable properties. In particular, epitaxial QD lasers directly grown on silicon have recently led to record performance such as ultra-low threshold currents, high temperature continuous-wave operation, very long device lifetimes as well as high yield and much better scalability³. In addition, the use of p-doping significantly improves their thermal stability and reliability⁷. It also reduces the linewidth enhancement factor (α -factor), resulting in reflection insensitivity, which is of vital importance for isolator-free PICs⁸. Extending these advances to integrated photonics technologies will lead to silicon platforms with on-chip nonclassical light sources, large versatile photonic logic, quantum information storage, and highly efficient detectors⁹.

Four-wave mixing (FWM) is useful in optical communications for all-optical signal processing and for wavelength-division multiplexing (WDM) systems, which are a key component in coherent communication technologies¹⁰⁻¹². FWM is known to drive the phase and mode-locking properties observed in comb QD lasers^{13,14}. Therefore, our interest in FWM susceptibility involves QD lasers, where mode locking is possible with both single- and multi-section diode lasers^{13,15}. The interest comes from applications in telecom and datacom. For example, in the case of WDM systems, a single mode locked laser producing a frequency comb can potentially replace the large number of lasers presently necessary for the task. A single-section mode-locked laser using self-mode locking amplifies the advantages even further. However, there are serious challenges because with self-mode locking, the gain medium alone has to produce the multimode lasing that leads to broad emission bandwidth, and the FWM contributes to the locking of the frequencies. Within the inhomogeneously broadened distribution of QDs, the optical nonlinearities of light-matter interactions give rise to both mechanisms. To control self-mode locking to the extent that it can be employed in applications, such as WDM, requires a deeper understanding than we have presently of the intricate interplay of physics associated with mode competition and FWM. Our laser experiments and accompanying theoretical analysis are designed with exactly that goal in mind.

Within a nonlinear gain medium that has a third-order nonlinear susceptibility, the beating between two co-polarized fields at different frequencies results in the occurrence of wave-mixing and the generation of two new fields. The highly nonlinear optical fibers are certainly good candidates for achieving efficient wave-mixing conversion, however, the required interaction length of several meters together with the large pump power makes them not suitable for monolithic integration^{16,17}. To overcome this limit, efficient FWM with relatively low power consumption can also be achieved with micro-ring resonators, however, at the price of implementing sophisticated low-loss bus waveguide designs¹⁸⁻²⁰. In addition, high fabrication costs may be another issue compared with more compact devices, such as semiconductor optical amplifier (SOA) or semiconductor laser sources. In the latter case, the FWM is essentially driven by the carrier density pulsation (CDP) which reinforces the wave-mixing conversion efficiency, nevertheless, the nanosecond timescale of the carrier recombination lifetime leads to a slow response speed²¹. In this context, as compared to bulk and quantum well (QW) semiconductors, QDs exhibit larger optical nonlinearities with

faster response speed. The QD gain material is spectrally broader, and the fast carrier dynamics along with the lower linewidth enhancement factor improves the conversion efficiency²². Prior work concentrated on QD SOAs^{23,24} and lasers^{25,26} grown on lattice matched substrates. In the former, although the higher conversion efficiency can be achieved through the larger linear gain in SOAs, the inherently stronger amplified spontaneous emission noise limits the optical signal-to-noise ratio.

This paper reports recent results from a study aim at understanding FWM in QD lasers epitaxially grown on silicon, taking into account their enhanced cavity resonances and reduced amplified spontaneous emission noise. In our investigation, we measured and analyzed the nonlinear optical contributions resulting in mode competition, gain saturation, carrier-induced refractive index, α -factor and creation of combination tones, all of which have roles in self-mode-locking. The experiments were performed on epitaxial QD lasers with inhomogeneous broadening below 10 meV, similar to ones that we used to achieve frequency combs with RF linewidth less than 100 kHz and mode-locked pulse below 500 fs¹³. The present motivation is to build on prior results and to confirm that the contributing nonlinearities in general combine to provide a strong mechanism of self-mode-locking. Success will significantly reduce complexity and energy requirement in WDM systems.

2 Device description

The Fabry-Perot (FP) QD laser material was grown a 300 mm on-axis (001) GaP/Si substrate. The active region includes five periods of QD layers. The dot-in-a-well QD layer composed of InGaAs QWs asymmetrically encompassing the InAs dots with a 2 nm prelayer below and a 5 nm capping layer on the top. Each QD layer is separated by a 37.5 nm GaAs spacer. For p-doped QD lasers, a 10 nm p-GaAs layer at a target hole concentration of $5 \times 10^{17} \text{ cm}^{-3}$ (10 extra holes per QD) is sandwiched between a 10 nm undoped GaAs layer and a 17.5 nm undoped GaAs layer. It is noted that the gain is temperature sensitive in QD laser due to the thermal spreading of holes. To solve this problem, the p-doping in the GaAs spacer can counter the influence of closely spaced whole energy level hence the ground state transition of QD is full of holes. The inclusion of p-doping brings many advantages for laser devices. On the one hand, the p-doping can ease the thermal spread of holes and lead to rather temperature-insensitive characteristics such as threshold current, α -factor, relative intensity noise and optical feedback resistance^{10,27,28}. On the other hand, it can also eliminate gain saturation and gain broadening, hence improving the high-frequency response of QD lasers^{29,30}. Furthermore, the optimized growth conditions contribute to a narrow photoluminescence full-width-at-half-maximum below 30 meV, which transforms an inhomogeneous broadening width of 10 meV⁸. The output facet has a facet coating of 60% power reflectivity while the rear facet has a value of 90%.

3 Four-wave mixing experiment

Fig. 1 depicts the FWM experimental setup with optical injection locking configuration. Two narrow linewidth tunable lasers are used as drive laser and probe laser, the light of which is incorporated by a 90/10 coupler and then injected into the QD laser using optical circulator and lens-end fiber. The drive laser is used to lock the gain peak mode of the FP modes while the probe laser is used to generate the FWM with the locked FP modes. The polarization controllers are applied to align the polarization of two tunable lasers with QD laser for realizing the maximum conversion. The FWM optical spectrum is recorded from the optical circulator by an optical spectrum analyzer (OSA) with a 20 pm resolution. The working temperature of the QD laser is kept at 293 K throughout the experiment using a thermoelectric cooler.

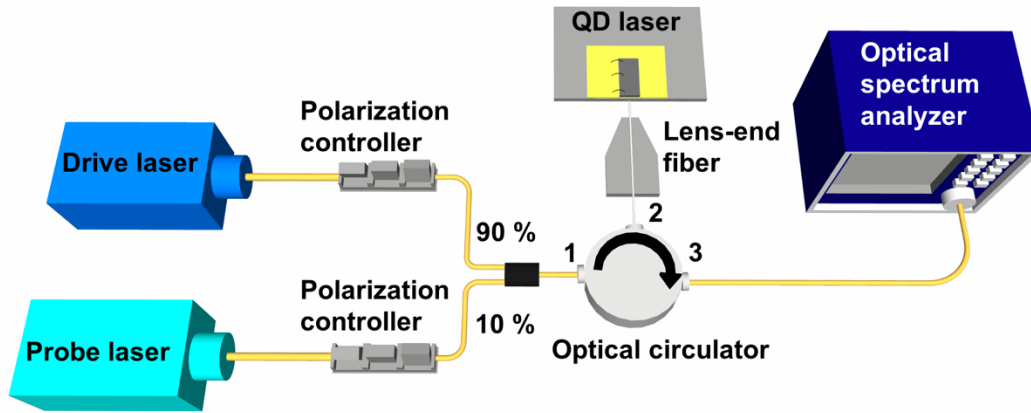


FIG. 1. Optical injection locking setup used for the four-wave mixing experiments.

The probe-drive injection frequency detuning Δ is defined as the frequency difference between the drive laser and probe laser. The drive laser is used to lock the longitudinal FP mode at the gain peak while the side modes are deeply suppressed, hence generating the drive signal for wave-mixing. Within the stable-locked regime, the frequency of the probe laser is then tuned to have the probe signal coincide with one of the suppressed FP cavity modes to obtain maximum conversion. Fig. 2(a) and 2(b) show typical FWM spectra recorded for undoped laser with $\Delta=114$ GHz and for p-doped laser with $\Delta=89$ GHz. It is noted that the free spectral range (FSR) is 38 GHz for the undoped laser and 30 GHz for the p-doped one. The middle peak represents the FP mode locked in the QD gain peak at the drive laser frequency with deeply suppressed sidemodes. The left peak is the probe signal mode while the right one is the wave-mixing induced converted signal. The different colored curves in Figs 2(a) and (b) show the signal power increase with increasing the probe power.

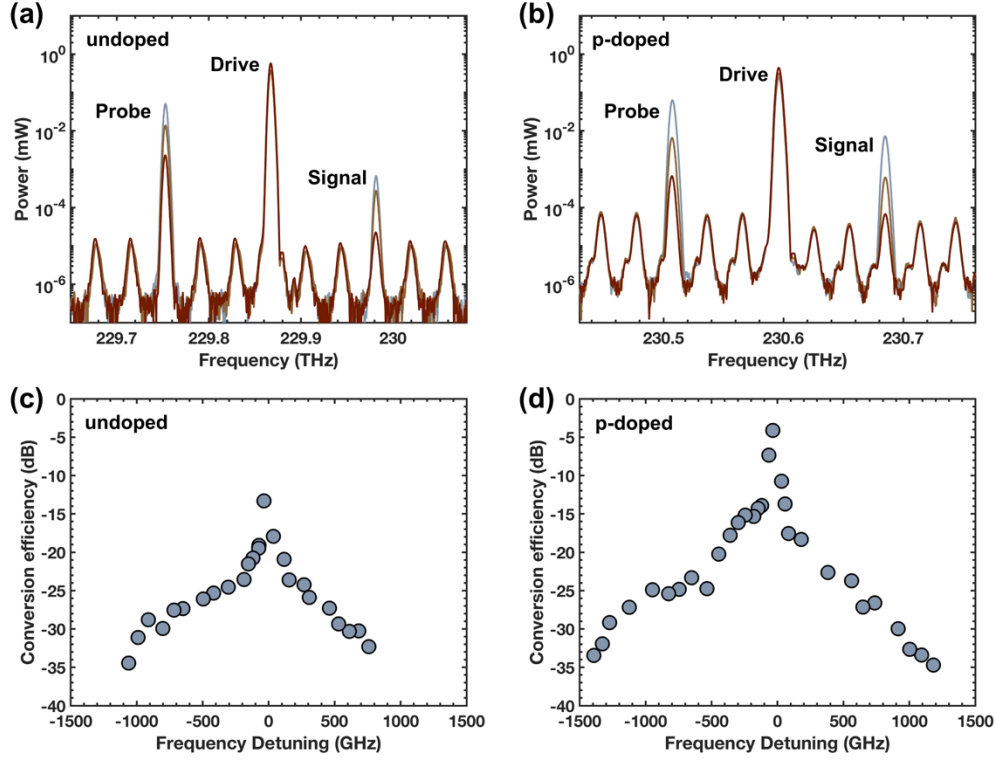


FIG. 2. Optical spectra from a four-wave mixing experiment for (a) undoped laser with up-conversion frequency detuning of 114 GHz and (b) p-doped laser with up-conversion frequency detuning of 89 GHz (probe-drive mode number difference $\Delta m = 3$). The different colored lines indicate signal power increase with increasing the probe power. Conversion efficiency of four-wave mixing for (c) undoped laser and (d) p-doped laser as a function of the probe-drive frequency detuning.

The conversion efficiency is expressed as²²:

$$\eta_{CE} = \frac{P_{Signal}}{P_{Probe}} \quad (1)$$

with P_{Signal} is the optical power of the converted signal and P_{Probe} is the probe signal power injected into the laser. In the experiment, these powers are obtained from the measured optical spectrum. The laser-fiber coupling loss is estimated by calculating the ratio between the laser free-space output power and the laser power coupled in the lens-end fiber. The total losses include coupling loss and fiber loss, which are considered in the spectra in order not to over-estimate the value of η_{CE} . The value of η_{CE} is expressed in logarithmic scale (in dB) in this paper.

In the first set of measurements, we keep the probe power constant, adjust the probe frequency by multiples of the FSR and record the resulting maximal η_{CE} for each FSR. Fig. 2(c) and 2(d) compare the measured η_{CE} for undoped and p-doped lasers as a function of the probe-drive injection frequency detuning. The up-conversion (down-conversion respectively) refers to the converted signal has a frequency higher (lower respectively) than the drive, hence the probe

frequency minus drive frequency is negative (positive respectively). As shown, the probe-drive injection frequency detunings at which η_{CE} is measured are multiples of the FSR of the FP laser and the corresponding η_{CE} are the local maxima. The maximal η_{CE} is found at -13 dB for the undoped laser and -4 dB for the p-doped laser when the probe laser injects into the first longitudinal mode next to the drive signal. These results are consistent with native InAs/GaAs QD laser while the maximal η_{CE} is a bit larger²². For the undoped laser, the η_{CE} is kept above -35 dB for up-conversion with frequency detunings up to 1 THz and up to 760 GHz for down-conversion. The frequency detunings for η_{CE} above -35 dB in p-doped laser are larger than that of the undoped laser, which are up to 1.4 THz for up-conversion and 1.2 THz for down-conversion. The larger maximal η_{CE} and frequency detuning in p-doped laser are due to the increased material gain because the p-doping eliminates gain saturation and gain broadening³¹. It is noted that the static conversion at low-frequency region is determined by the carrier density pulsation (CDP), which is directly caused by the probe-drive beating. For larger frequency detunings, carrier heating (CH) and spectral hole burning (SHB) become the dominant mechanisms occurring within sub-picosecond timescales. Although η_{CE} are higher at low frequency hence increasing the third-order nonlinear susceptibility, the very large bandwidth provided by the CH and SHB remain very promising for broadband wavelength conversion. The different bandwidth between up and down conversion is attributed to the asymmetry in the gain profile leading to a non-zero α -factor. In theory, with a zero α -factor, the bandwidths are perfectly symmetric. Although the α -factor is small in epitaxial QD lasers, destructive interferences still persist due to the phase condition arising between the different nonlinear processes (eg. CDP, CH and SHB). In addition, the profiles between up-conversion and down-conversion are found to be more symmetric in p-doped laser than that of undoped one, which is due to lower α -factor. As previously demonstrated, the α -factor of the p-doped laser is found to be as low as 0.13 at the gain peak, which is lower than that of the undoped laser with α -factor of 0.3²⁷.

4 Theory

Fig. 3(a) shows a drawing of the laser showing the QD active region, which consists of 5 layers of InGaAs QWs embedding InAs QDs and separated by GaAs barriers. A transverse waveguide is formed by AlGaAs cladding layers. For a FWM experiment, the injected intensities are I_d^{inj} and I_p^{inj} , the measured output intensities are I_d^{out} , I_p^{out} and I_s^{out} . The model computes the corresponding intracavity intensities I_d , I_p and I_s . Intensities in the other modes are I_n . Fig. 3(b) demonstrates the electronic states contributing to the laser transitions. The electronic states considered in the model are the ground and excited states from the QDs, and the continuum of states from the QWs. Laser transitions involve only the inhomogeneously broadened QD ground states. The laser modes participating in an intracavity FWM experiment are shown in Fig. 3(c).

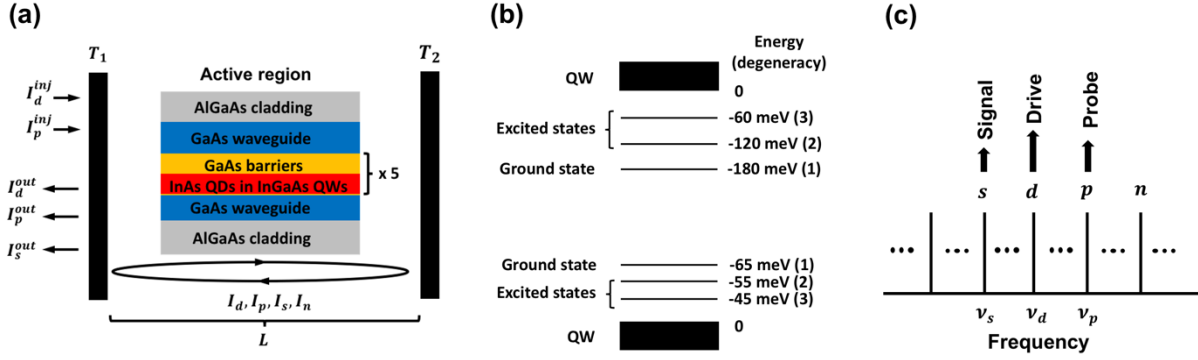


FIG. 3. (a) Sketch of laser showing QD active region inside optical cavity of length L and facet transmissions T_1 and T_2 . The active region consists 5 layers of InGaAs QWs embedding InAs QDs and separated by GaAs barriers. (b) Electronic states considered in the model are the ground and excited states from the QDs, and the continuum of states from the QWs. (c) Laser modes participating in an intracavity four-wave mixing experiment. Injections are at the drive and probe modes, labeled d and p , respectively. The signal appears in the mode labeled s . The model also tracks other lasing or nonlasing modes, collectively labeled as n .

To extract the FWM coefficient from the measured data, we developed a laser model for the intensity in cavity mode, as sketched in Fig.3(c). A semiclassical treatment³² is chosen to treat gain saturation, mode competition and multi-wave mixing on equal footing³³.

From the semiclassical derivation, the intracavity drive, probe and signal intensities evolve according to:

$$\frac{d}{dt} i_d = \left(g_d^{sat} - \frac{\nu_0}{Q} \right) i_d + \frac{c}{2Ln_b} \sqrt{T_1 i_d^{inj}} i_d + s \quad (2)$$

$$\frac{d}{dt} i_p = \left(g_p^{sat} - \frac{\nu_0}{Q} \right) i_p + \frac{c}{2Ln_b} \sqrt{T_1 i_p^{inj}} i_p + s \quad (3)$$

$$\frac{d}{dt} i_s = \left(g_s^{sat} - \frac{\nu_0}{Q} \right) i_s + \sqrt{2} |\theta_{sdpd}| i_d \sqrt{i_s i_p} + s \quad (4)$$

Additionally, the derivation gives for the other lasing and non-lasing modes:

$$\frac{d}{dt} i_n = \left(g_n^{sat} - \frac{\nu_0}{Q} \right) i_n + s \quad (5)$$

In the above equations, we define a dimensionless intensity:

$$i_j = \frac{2}{\varepsilon_0 c n_B} \left(\frac{\wp}{2\hbar\gamma} \right)^2 I_j \quad (6)$$

where ε_0 and c are the permittivity and speed of light in vacuum, n_B is the background refractive index, \wp is the QD dipole matrix element, γ is the dephasing rate and I_m is the intensity in the m^{th} cavity mode. Also in the equations, the cavity linewidth L is expressed in terms of an average cavity mode frequency ν_0 and the cavity quality factor Q :

$$\frac{\nu_0}{Q} = \frac{c}{n_b} \left[\alpha_{abs} - \frac{1}{2L} \ln(R_1 R_2) \right] \quad (7)$$

where α_{abs} is the intracavity absorption, $R_l = 1 - T_l$ and $R_r = 1 - T_r$. Each cavity mode experiences a saturated modal gain given by:

$$g_n^{sat} = \frac{g_n}{1 + \kappa_{nn}i_n + \sum_{m \neq n} \kappa_{n,m}i_m} \quad (8)$$

where g_n is the unsaturated (small signal) modal gain, κ_{nn} is the self-gain compression factor and $\kappa_{n,m}$ is the cross gain compression factor. To account for spontaneous we add s to Eqs. (2) - (5):

$$s = \frac{\hbar\nu_0\beta B_{2d}}{2\varepsilon_0 n_b^2 d_{qw}} \left(\frac{\wp}{2\hbar\gamma}\right)^2 n_{e0}n_{h0} \quad (9)$$

where β is the spontaneous emission factor, B_{2d} is the bimolecular carrier recombination coefficient, d_{qw} is the thickness of each QW layer embedding the QDs, n_{e0} and n_{h0} are the carrier densities in the QD electron and hole ground states.

The gain parameters g_n , κ_{nn} and $\kappa_{n,m}$ depend on carrier densities. We group the electron and hole densities into those populating the inhomogeneously broadened QD ground states n_{e0} and n_{h0} , those populating the QD excited states n_{e1} and n_{h1} , and those populating the QW layers n_{e2} and n_{h2} . The semiclassical laser theory also provides the following equations of motion for the carrier densities:

$$\frac{dn_{e0}}{dt} = -\frac{\varepsilon_0 n_b^2 d_{qw}}{\hbar\nu_0 \Gamma_{conf}} \left(\frac{2\hbar\gamma}{\wp}\right)^2 \sum_n g_n^{sat} i_n - \gamma_r (n_{e0} - n_{e0}^{eq}) - B_{2d} n_{e0} n_{h0} - \gamma_{nr} n_{e0} - C_{2d} n_{e0}^2 n_{h0} \quad (10)$$

$$\frac{dn_{h0}}{dt} = -\frac{\varepsilon_0 n_b^2 d_{qw}}{\hbar\nu_0 \Gamma_{conf}} \left(\frac{2\hbar\gamma}{\wp}\right)^2 \sum_n g_n^{sat} i_n - \gamma_r (n_{h0} - n_{h0}^{eq}) - B_{2d} n_{e0} n_{h0} - \gamma_{nr} n_{h0} - C_{2d} n_{e0} n_{h0}^2 \quad (11)$$

$$\frac{dn_{e1}}{dt} = -\gamma_r (n_{e1} - n_{e1}^{eq}) - B_{2d} n_{e1} n_{h1} - \gamma_{nr} n_{e1} - C_{2d} n_{e1}^2 n_{h1} \quad (12)$$

$$\frac{dn_{h1}}{dt} = -\gamma_r (n_{h1} - n_{h1}^{eq}) - B_{2d} n_{e1} n_{h1} - \gamma_{nr} n_{h1} - C_{2d} n_{e1} n_{h1}^2 \quad (13)$$

$$\frac{dn_{e2}}{dt} = \frac{\eta J}{e} - \gamma_r (n_{e2} - n_{e2}^{eq}) - B_{2d} n_{e2} n_{h2} - \gamma_{nr} n_{e2} - C_{2d} n_{e2}^2 n_{h2} \quad (14)$$

$$\frac{dn_{h2}}{dt} = \frac{\eta J}{e} - \gamma_r (n_{h2} - n_{h2}^{eq}) - B_{2d} n_{e2} n_{h2} - \gamma_{nr} n_{h2} - C_{2d} n_{e2} n_{h2}^2 \quad (15)$$

The first terms on the right-hand side of Eqs. (10) and (11) are from stimulated emission, where Γ_{conf} is the mode confinement factor. The terms with an effective carrier scattering rate γ_r approximate carrier relaxation of all the states towards quasi-equilibrium. The quasi-equilibrium densities n_α^{eq} are determined by the conservation of carrier population. We assume equilibrium within each density group. However, in general, $n_\alpha \neq n_\alpha^{eq}$ because of dynamic population bottleneck. Details on implementing this phenomenological approach to modeling carrier scattering effects and its accuracy compared to quantum kinetic calculations are discussed in earlier publications^{34,35}. Also in the carrier density equations are the carrier loss contributions. The terms with γ_{nr} and C_{2d} account for carrier losses from defect and Auger scattering, respectively. Lastly, in Eqs. (14) and (15), J is the injected current density and η is the injection efficiency from electrodes to QW states.

The saturated gain in Eq. (8) is determined using the following expressions. Starting with the small signal gain, semiclassical laser theory gives:

$$g_n = [f_{e0,n} + f_{h0,n} - 1] \frac{\nu_0 \wp^2 N_{qd} \Gamma_{conf}}{\epsilon_0 n_b^2 \hbar \gamma d_{qw}} \Lambda_n \quad (16)$$

where

$$\Lambda_n = \int_{-\infty}^{\infty} d\omega \frac{1}{\sqrt{2\pi}\Delta_{inh}} \exp\left[-\left(\frac{\omega-\omega_0}{\sqrt{2}\Delta_{inh}}\right)^2\right] L(\omega - \nu_n) \quad (17)$$

$$L(\omega - \nu_n) = \frac{\gamma^2}{\gamma^2 + (\omega - \nu_n)^2} \quad (18)$$

and the quantity inside the square bracket is the population inversion, assuming equilibrium among QD ground state populations within the inhomogeneously broadened distribution of width Δ_{inh} . The quantities $f_{e0,n}$ and $f_{h0,n}$ are Fermi functions evaluated for the QD populations contributing to the lasing transition at frequency ν_n , based on the instantaneous QD ground state densities n_{e0} and n_{h0} .

Semiclassical laser theory also gives the self- and cross- gain compression factors:

$$\kappa_n = 3 \frac{\gamma}{\gamma_{ab}} \frac{1}{\Lambda_n} \int_{-\infty}^{\infty} d\omega \frac{1}{\sqrt{2\pi}\Delta_{inh}} \exp\left[-\left(\frac{\omega-\omega_0}{\sqrt{2}\Delta_{inh}}\right)^2\right] L^2(\omega - \nu_n) \quad (19)$$

$$\kappa_{n,m} = \frac{\gamma}{\gamma_{ab}} \left(1 + \frac{\zeta_{nm}}{2}\right) \frac{1}{\Lambda_n} \int_{-\infty}^{\infty} d\omega \frac{1}{\sqrt{2\pi}\Delta_{inh}} \exp\left[-\left(\frac{\omega-\omega_0}{\sqrt{2}\Delta_{inh}}\right)^2\right] \left\{2L(\omega - \nu_n)L(\omega - \nu_m) + \text{Re}\{D_{\gamma_{ab}}(\nu_m - \nu_n)D_{\gamma}(\omega - \nu_n)[D_{\gamma}(\nu_m - \omega) + D_{\gamma}(\nu_n - \omega)]\}\right\} \quad (20)$$

where

$$D_{\alpha}(\chi) = \frac{\alpha}{\alpha + i\chi} \quad (21)$$

and ζ_{nm} accounts for the effects of spatial hole burning in the presence of carrier diffusion. In the limit of no carrier diffusion,

$$\zeta_{nm} = \frac{1}{L} \int_0^L dz \cos[2(k_n - k_m)z] = \delta_{n,m} \quad (22)$$

If carrier diffusion dominates, $\zeta_{nm} = 1$ for all combinations of n and m . The focus on our investigation is on the relative phase angle term³² in Eq. (4), which contributes to the signal intensity via FWM.

To extract the FWM susceptibility for mode locking $\chi_{sdpd}^{(3)}$, we solve Eqs. (2) - (5) and Eqs. (10) - (15), with the relative phasing angle coefficient θ_{sdpd} as an input parameter. The value of θ_{sdpd} that best fit the experimental data then gives the susceptibility:

$$\chi_{sdpd}^{(3)} = \frac{\sqrt{2}n_b}{\nu_0 \Gamma_{conf}} \left(\frac{\wp}{2\hbar\gamma}\right)^2 |\theta_{sdpd}| \quad (23)$$

In an earlier study,^{36,37} a first-principle based multimode laser theory was used to derive the following expression for the relative phase angle coefficient:

$$|\theta_{sdpd}| = (f_{e,s} + f_{h,s} - 1) \frac{\nu_0 \wp^2 N_{QD}^{(2d)} \Gamma_{conf}}{2\epsilon_0 n_b^2 \hbar \gamma d_{qw}} \frac{\gamma}{\gamma_{ab}} \frac{1}{2} (1 + 2\zeta)$$

$$\begin{aligned} & \times \int_{-\infty}^{\infty} d\omega \frac{1}{\sqrt{2\pi}\Delta_{inh}} e^{-\left[\frac{\omega-\omega_0}{\sqrt{2}\Delta_{inh}}\right]^2} \\ & \times |D_\gamma(\omega + v_p - 2v_d)D_{\gamma_{ab}}(v_p - v_d)[D_\gamma(v_p - \omega) + D_\gamma(\omega - v_d)]| \end{aligned} \quad (24)$$

A quantity that is often extracted from experiments is $\chi_{sdpd}^{(3)}$ divided by the material small signal gain in inverse length^{25,38}. One can see the attractiveness by using Eqs. (16), (23) and (24) to obtain:

$$\begin{aligned} \xi & \equiv \chi_{sdpd}^{(3)} \frac{c\Gamma_{conf}}{n_b g_s} \\ & = \frac{\sqrt{2}c}{v_0\Lambda_s} \left(\frac{\wp}{2\hbar\gamma}\right)^2 \frac{\gamma}{\gamma_{ab}} \frac{1}{2} (+2\zeta) \times \int_{-\infty}^{\infty} d\omega \frac{1}{\sqrt{2\pi}\Delta_{inh}} e^{-[(\omega-\omega_0)/\sqrt{2}\Delta_{inh}]^2} \\ & \times |D_\gamma(\omega + v_p - 2v_d)D_{\gamma_{ab}}(v_p - v_d)[D_\gamma(v_p - \omega) + D_\gamma(\omega - v_d)]| \end{aligned} \quad (25)$$

The results show a quantity that depends only on the electronic structure and broadenings associated with carrier scattering. Its generality arises from being independent of the laser configuration, in terms of confinement factor, QD density, heterostructure layer thicknesses and injection current.

TABLE I. Device parameters. † Computed for QW embedding QDs.

Device parameter	Symbol	Value
QD layers	n_{qd}	5
QD density	N_{qd}	$4 \times 10^{14} m^{-2}$
QD layer thickness	d_{qw}	7 nm
Barrier thickness	d_b	40 nm
Waveguide cross section	$w \times d_{wg}$	$4.9 \mu m \times 0.3 \mu m$
Cavity length	L	1.1 mm
Facet reflections	R_1, R_2	0.6, 0.9
Mode spacing	Δ_c	38 GHz undoped 30 GHz p-doped
Inhomogeneous width	Δ_{inh}	10 meV
Mode confinement factor	Γ_{conf}	0.06 †

TABLE II. Model input parameters. † Based on $C_{2d} = C_{3d}/d_{qw}^2$ with $C_{3d} = 1.7 \times 10^{-38} m^6 s^{-1}$.

Model parameter	Symbol	Value
Dephasing rate	γ	$10^{13} s^{-1}$
QD-QW scattering rate	γ_r	$10^{13} s^{-1}$

Inter-QD scattering rate	γ_{ab}	$5 \times 10^{11} \text{ s}^{-1}$
Defect loss rate	γ_{SRH}	$4 \times 10^8 \text{ s}^{-1}$ undoped $2 \times 10^9 \text{ s}^{-1}$ p-doped
Bimolecular recombination coefficient	B_{2d}	$1.4 \times 10^{-8} \text{ m}^2 \text{ s}^{-1}$
Auger coefficient [†]	C_{2d}	$3.5 \times 10^{-22} \text{ m}^4 \text{ s}^{-1}$
Spontaneous emission factor	β	10^{-3}
Intracavity absorption	α_{abs}	1200 m^{-1} undoped 1600 m^{-1} p-doped
Spatial hole burning	ξ	0.5

Before using the model to extract $\chi_{sdpd}^{(3)}$, we need to determine the values for its input parameters. First are the device parameters determined through fabrication. These parameters are listed in Table I and their values are entered directly into the model. Then come the model parameters that are in Table II. From the list, the spontaneous emission and Auger coefficients B_{2d} and C_{2d} , respectively, are from published data^{39,40}. The reminders are determined by anchoring computed laser behavior to measured ones, as discussed below.

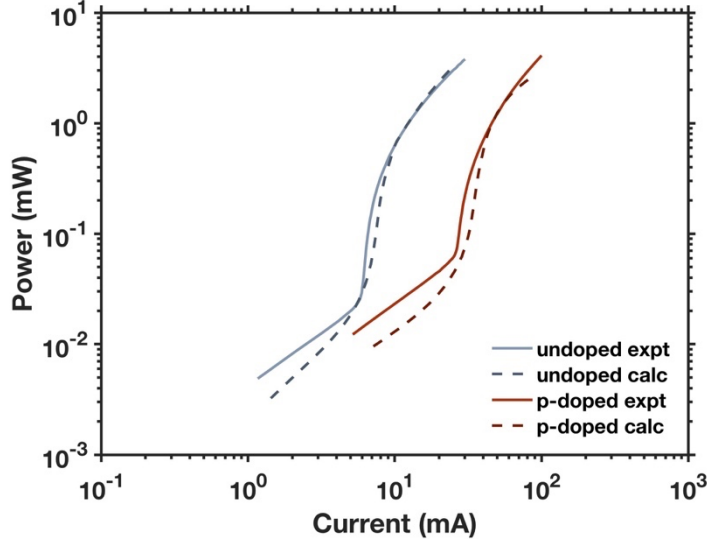


FIG. 4. Output power versus current for undoped and p-doped lasers used in four-wave mixing experiments. The solid lines are the experimental results and the dashed lines are the simulation. Input parameters for the calculated curves are given in Table II.

Fig. 4 presents the output power as a function of bias current of both undoped and p-doped QD lasers used in the study. The undoped laser has threshold current of 6 mA at 293 K, while the p-doped laser has a bit larger threshold current of 27 mA due to the high free carrier absorption caused by the large number of holes. The dashed lines are from the theoretical calculation using the device and gain medium parameters listed in Tables I and II. Both lasers have ground state

emission at 1.3 μm . The fitting of power-current curves pins the intracavity absorption α_{abs} , injection efficiency η and defect (SRH) loss rate γ_{nr} . We note that the higher intracavity absorption and defect loss rate with p-doping is consistent with previous studies on p-doping effects³¹. The p-doping changes linear and nonlinear gain properties through state filling and carrier scattering induced dephasing, as well as alters the γ_{nr} and α_{abs} ³¹. These effects are taken into account in the model.

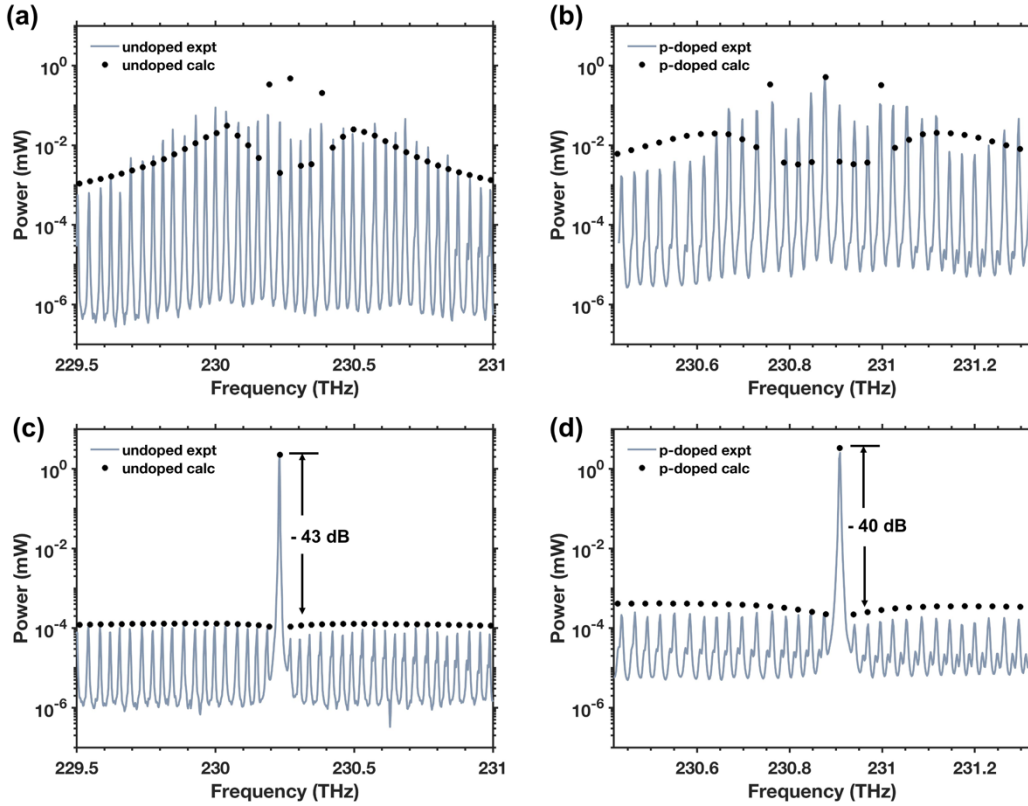


FIG. 5. Measured optical spectra from undoped (a) free-running and (c) injection-locked lasers operating at twice threshold current. Measured optical spectra from p-doped (b) free-running and (d) injection-locked lasers operating at twice threshold current. The points are the calculated mode power.

Optical spectra of both lasers under free running and injection-locked operating at twice threshold current are shown in Fig. 5. When fitting to the free-running lasing spectra in Fig. 5(a) and 5(b), we observed a transition from a smooth multimode frequency comb to a spiky one with increasing current. As the transition is caused by mode competition, we believe that it is more important to reproduce this excitation dependent transition than the actual spectral shape. Doing so fixes the scattering rates γ , γ_r and γ_{ab} . The chosen values for γ and γ_r are consistent with those from quantum kinetic calculations⁴¹. The spectral fit also specifies the spatial hole burning parameter. We found that a value of $\zeta = 0.5$, midway between maximal and negligible carrier diffusion effects, to provide reasonable description of the measurements.

The final confirmation of the input parameters is from reproducing the spectra for the injection-locked lasers without any further adjustment of parameters. As shown in the Figs. 5(c) and 5(d), the model correctly describes the 43 dB and 40 dB side mode suppression for the undoped and p-doped lasers, respectively.

5 Extracting four-wave mixing coefficient

Due to their fast carrier-carrier and carrier-phonon scatterings, QDs have shown large optical nonlinearities and the fast FWM conversion has been achieved in QD SOAs as a result of fast carrier scattering induced deeper spectral holes³¹. The optical nonlinearities of epitaxial QD lasers on silicon are now analyzed based on a microscopic level model containing quantum mechanical electron-hole polarization^{36,37}. To do so, the net FWM coefficient (normalized to the material gain) $\xi \equiv \chi_{sdpd}^{(3)}/g_s$ is extracted from probe-drive laser experiment and connected to multimode semiclassical laser theory by considering the gain competition. We repeat the measurement giving the spectra in Figs. 2(a) and 2(b) for a range of probe power and for three different frequency detuning between drive and probe fields. The points in Figs. 6 summarize the experimental results and show the measured signal power with increasing probe power for fixed drive power. The plotted solid curves are obtained from the model with the relative phase angle coefficient θ_{sdpd} as a fitting parameter, which is chosen to bound the experimental points. The model simulations are in good agreement with the experiment results. For up to 4 mode number separation Δm between probe and drive fields in both undoped laser and p-doped lasers, we found the experimental points to be bounded by the choice of θ_{sdpd} giving $\xi \equiv \chi_{sdpd}^{(3)}/g_s$ between 4 and $8 \times 10^{-21} m^3 V^{-2}$. With higher separations, the extracted ξ falls below $4 \times 10^{-21} m^3 V^{-2}$.

Within the variance in the measured data, both undoped and p-doped lasers have basically the same values for ξ . However, as shown in Fig.6, the gain in signal power with increasing probe power (slope of data points and curves) indicates higher net FWM gain with p-doping. These results emphasize the need to consider gain competition and $\chi_{sdpd}^{(3)}$ on equal footing and under similar experimental conditions when evaluating mode-locking performance. Hence, caution should be exercised when drawing conclusions using only $\chi_{sdpd}^{(3)}$ measured in amplifier experiments. Rather, measurements should be made directly with lasers with configurations closely resembling the lasers one is attempting to mode lock. Along with fitting to experimental data, we also computed the conversion efficiency between the signal and drive power using a first-principle based multimode laser theory. It gives the relative phase angle coefficient as described in Eq. (24). The dashed curves show the theoretical prediction for the conversion efficiency as a function of ratio between probe and drive power. Comparison of theory and experiment indicates that the FWM susceptibility from our samples is consistent with the theoretical predictions.

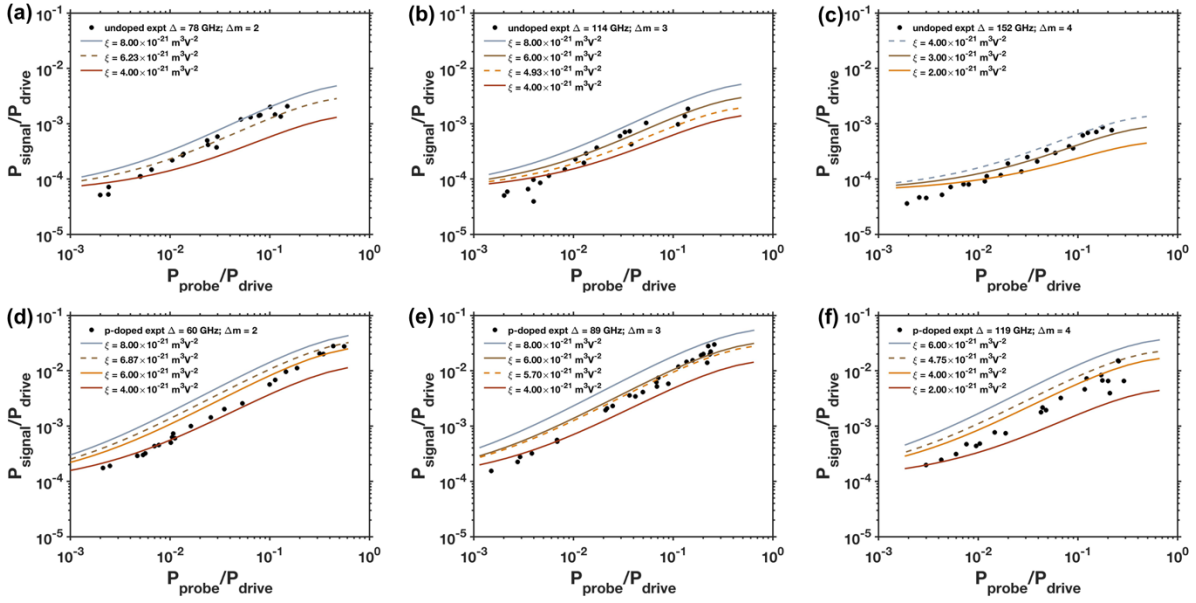


FIG. 6. Signal power versus probe power for (a, b, c) undoped and (d, e, f) p-doped lasers operating at twice threshold current. Both powers are normalized to the drive power. The data points are from experiment with probe-drive injection frequency detuning Δ as indicated. The calculated curves in (a, d) are for probe-drive mode number difference $\Delta m = 2$, that in (b, e) are for probe-drive mode number difference $\Delta m = 3$, and that in (c, f) are for probe-drive mode number difference $\Delta m = 4$. The dashed curves are computed using $\xi = \chi^{(3)}/g$ calculated from multimode laser theory. The other curves use ξ is an input parameter.

5 Conclusions and perspectives

In conclusion, we investigated the nonlinear optical properties in semiconductor QD lasers directly grown on silicon. Our experiments show strong optical nonlinearities that allow demonstration of self-mode-locking in lasers fabricated for use in silicon-based PICs. Gain saturation, mode competition and multi-wave mixing are connected through the active region optical nonlinearities, with the leading contribution arising from the third-order electron-hole polarization. In contrast to amplifier experiments, the probe-drive laser measurements provide valuable insight to the intricate interplay of optical nonlinearities during device operation. We show that the gain in signal power with increasing the probe power produces a much higher net FWM gain, the latter being even further magnified owing to p-doping. However, when the FWM gain is no longer enough to overcome the mode competition, the signal power drops. On the top of that, at large FWM susceptibility, the FWM gain can exceed the cavity losses hence lasing by FWM can take place. Consequently, the laser experiments provide clear differences from the amplifier ones because of the gain saturation by the drive and probe intracavity fields.

While epitaxial QD lasers on silicon are already strong building blocks of on-chip integrated quantum photonic circuits^{42,43}, further analysis could possibly extend this work to semiconductor-based quantum information systems. For instance, the high third-order nonlinear susceptibility can be used for light squeezing to reduce the noise below the standard quantum limit^{44,45}. Squeezed states can be generated by using a FWM source made with epitaxial QDs⁴⁶. Overall, these results allow us to present the new insights of the third order non-linearity for the mode locking mechanism of the QDs comb laser, which is crucial for classical coherent communication. The experiments are solid and quantitatively compared to the microscopic model. It could also pave the way for the control of optical nonlinearities in epitaxial QDs at the crossway between classical and quantum physics in the future.

Acknowledgements

This work is supported in part by the Center for Integrated Nanotechnologies (CINT) through a Rapid Access proposal (2019BRA0032). Authors also acknowledge the financial support of the DARPA PIPES program, the Institut Mines-Télécom, and the Research Startup Fund of HITSZ.

Conflict of interests

The authors declare no conflict of interest.

References:

- 1 Elshaari, A. W., Pernice, W., Srinivasan, K., Benson, O., & Zwiller, V. Hybrid integrated quantum photonic circuits. *Nat. Photonics*, 1-14 (2020).
- 2 Helkey, R., Saleh, A. A., Buckwalter, J., & Bowers, J. E. High-performance photonic integrated circuits on silicon. *IEEE J. Sel. Top. Quantum Electron.*, 25(5), 1-15 (2019).
- 3 Norman, J. C., Jung, D., Zhang, Z., Wan, Y., Liu, S., Shang, C., ... & Bowers, J. E. A review of high-performance quantum dot lasers on silicon. *IEEE J. Quantum Electron.*, 55(2), 1-11(2019).
- 4 Liao, M., Chen, S., Liu, Z., Wang, Y., Ponnampalam, L., Zhou, Z., ... & Snowton, P. M. Low-noise 1.3 μm InAs/GaAs quantum dot laser monolithically grown on silicon. *Photonics Research*, 6(11), 1062-1066 (2018).
- 5 Nishi, K., Takemasa, K., Sugawara, M., & Arakawa, Y. Development of quantum dot lasers for data-com and silicon photonics applications. *IEEE J. Sel. Top. Quantum Electron.*, 23(6), 1-7 (2017).
- 6 Zhang, C., Liang, D., Kurczveil, G., Descos, A., & Beausoleil, R. G. Hybrid quantum-dot microring laser on silicon. *Optica*, 6(9), 1145-1151(2019).
- 7 Norman, J. C., Zhang, Z., Jung, D., Shang, C., Kennedy, M. J., Dumont, M., ... & Bowers, J. E. The importance of p-doping for quantum dot laser on silicon performance. *IEEE J. Quantum Electron.*, 55(6), 1-11(2019).

- 8 Grillot, F., Norman, J. C., Duan, J., Zhang, Z., Dong, B., Huang, H., ... & Bowers, J. E. Physics and applications of quantum dot lasers for silicon photonics. *Nanophotonics*, 9(6): 1271–1286 (2020).
- 9 Norman, J. C., Jung, D., Wan, Y., & Bowers, J. E. Perspective: The future of quantum dot photonic integrated circuits. *APL Photonics*, 3(3), 030901 (2018).
- 10 Chow, W. W., & Jahnke, F. On the physics of semiconductor quantum dots for applications in lasers and quantum optics. *Progress in Quantum Electron.*, 37(3), 109-184 (2013).
- 11 Stern, B., Zhu, X., Chen, C. P., Tzuang, L. D., Cardenas, J., Bergman, K., & Lipson, M. On-chip mode-division multiplexing switch. *Optica*, 2(6), 530-535 (2015).
- 12 Cheng, Q., Bahadori, M., Glick, M., Rumley, S., & Bergman, K. Recent advances in optical technologies for data centers: a review. *Optica*, 5(11), 1354-1370 (2018).
- 13 Liu, S., Jung, D., Norman, J. C., Kennedy, M. J., Gossard, A. C., & Bowers, J. E. 490 fs pulse generation from passively mode-locked single section quantum dot laser directly grown on on-axis GaP/Si. *Electron. Lett.*, 54(7), 432-433 (2018).
- 14 Dong, B., Huang, H., Duan, J., Kurczveil, G., Liang, D., Beausoleil, R. G., & Grillot, F. Frequency comb dynamics of a 1.3 μm hybrid-silicon quantum dot semiconductor laser with optical injection. *Opt. Lett.*, 44(23), 5755-5758 (2019).
- 15 Huang, X., Stintz, A., Li, H., Lester, L. F., Cheng, J., & Malloy, K. J. Passive mode-locking in 1.3 μm two-section InAs quantum dot lasers. *Appl. Phys. Lett.*, 78(19), 2825-2827 (2001).
- 16 Lee, J. H., Belardi, W., Furusawa, K., Petropoulos, P., Yusoff, Z., Monroe, T. M., & Richardson, D. J. Four-wave mixing based 10-Gb/s tunable wavelength conversion using a holey fiber with a high SBS threshold. *IEEE Photonics Tech. Lett.*, 15(3), 440-442 (2003).
- 17 Tuan, T. H., Cheng, T., Asano, K., Duan, Z., Gao, W., Deng, D., ... & Ohishi, Y. Optical parametric gain and bandwidth in highly nonlinear tellurite hybrid microstructured optical fiber with four zero-dispersion wavelengths. *Opt. Express*, 21(17), 20303-20312 (2013).
- 18 Ferrera, M., Razzari, L., Duchesne, D., Morandotti, R., Yang, Z., Liscidini, M., ... & Moss, D. J. Low-power continuous-wave nonlinear optics in doped silica glass integrated waveguide structures. *Nat. Photonics*, 2(12), 737-740 (2008).
- 19 Ferrera, M., Duchesne, D., Razzari, L., Peccianti, M., Morandotti, R., Cheben, P., ... & Moss, D. J. Low power four wave mixing in an integrated, micro-ring resonator with Q= 1.2 million. *Opt. Express*, 17(16), 14098-14103 (2009).
- 20 Ong, J. R., Kumar, R., Aguinaldo, R., & Mookherjea, S. Efficient CW four-wave mixing in silicon-on-insulator micro-rings with active carrier removal. *IEEE Photonics Tech. Lett.*, 25(17), 1699-1702 (2013).
- 21 Agrawal, G. P. Population pulsations and nondegenerate four-wave mixing in semiconductor lasers and amplifiers. *JOSA B*, 5(1), 147-159 (1988).
- 22 Huang, H., Arsenijević, D., Schires, K., Sadeev, T., Erasme, D., Bimberg, D., & Grillot, F. Efficiency of four-wave mixing in injection-locked InAs/GaAs quantum-dot lasers. *AIP Adv.*, 6(12), 125105 (2016).

- 23 Akiyama, T., Kuwatsuka, H., Simoyama, T., Nakata, Y., Mukai, K., Sugawara, M., ... & Ishikawa, H. Nonlinear gain dynamics in quantum-dot optical amplifiers and its application to optical communication devices. *IEEE J. Quantum Electron.*, 37(8), 1059-1065 (2001).
- 24 Ishikawa, H. Applications of quantum dot to optical devices. *Semiconductors and Semimetals*, 60, 287-324 (1999).
- 25 Su, H., Li, H., Zhang, L., Zou, Z., Gray, A. L., Wang, R., ... & Lester, L. F. Nondegenerate four-wave mixing in quantum dot distributed feedback lasers. *IEEE Photonics Tech. Lett.*, 17(8), 1686-1688 (2005).
- 26 Sadeev, T., Huang, H., Arsenijević, D., Schires, K., Grillot, F., & Bimberg, D. Highly efficient non-degenerate four-wave mixing under dual-mode injection in InP/InAs quantum-dot and quantum-dot lasers at 1.55 μm . *Appl. Phys. Lett.*, 107(19), 191111 (2015).
- 27 Duan, J., Huang, H., Jung, D., Zhang, Z., Norman, J., Bowers, J. E., & Grillot, F. Semiconductor quantum dot lasers epitaxially grown on silicon with low linewidth enhancement factor. *Appl. Phys. Lett.*, 112(25), 251111 (2018).
- 28 Duan, J., Zhou, Y., Dong, B., Huang, H., Norman, J. C., Jung, D., ... & Grillot, F. Effect of p-doping on the intensity noise of epitaxial quantum dot lasers on silicon. *Opt. Lett.*, 45(17), 4887-4890 (2020).
- 29 Deppe, D. G., Huang, H., & Shchekin, O. B. Modulation characteristics of quantum-dot lasers: The influence of p-type doping and the electronic density of states on obtaining high speed. *IEEE J. Quantum Electron.*, 38(12), 1587-1593 (2002).
- 30 Crowley, M. T., Naderi, N. A., Su, H., Grillot, F., & Lester, L. F. GaAs-based quantum dot lasers. In *Semiconductors and Semimetals* (Vol. 86, pp. 371-417). Elsevier (2012).
- 31 Zhang, Z., Jung, D., Norman, J. C., Patel, P., Chow, W. W., & Bowers, J. E. Effects of modulation p doping in InAs quantum dot lasers on silicon. *Appl. Phys. Lett.*, 113(6), 061105 (2018).
- 32 Sargent III, M., Scully, M. O., & Lamb Jr, W. E. (1974). *Laser Physics* Addison-Wesley. Reading, Mass (1974).
- 33 Nielsen, D., & Chuang, S. L. . Four-wave mixing and wavelength conversion in quantum dots. *Phys. Rev. B*, 81(3), 035305 (2010).
- 34 Chow, W. W., & Koch, S. W. Theory of semiconductor quantum-dot laser dynamics. *IEEE J. Quantum Electron.*, 41(4), 495-505 (2005).
- 35 Waldmueller, I., Chow, W. W., Young, E. W., & Wanke, M. C. Nonequilibrium many-body theory of intersubband lasers. *IEEE J. Quantum Electron.*, 42(3), 292-301 (2006).
- 36 Chow, W. W., Liu, S., Zhang, Z., Bowers, J. E., & Sargent, M. Multimode description of self-mode locking in a single-section quantum-dot laser. *Opt. Express*, 28(4), 5317-5330 (2020).
- 37 Grillot, F., Duan, J., Dong, B., Huang, H., Liu, S., Chow, W. W., ... & Bowers, J. E. Quantum dot lasers based photonics integrated circuits. In *2020 IEEE Photonics Conference (IPC)* (pp. 1-2). IEEE (2020).

- 38 Huang, H., Schires, K., Poole, P. J., & Grillot, F. Non-degenerate four-wave mixing in an optically injection-locked InAs/InP quantum dot Fabry–Perot laser. *Appl. Phys. Lett.*, 106(14), 143501 (2015).
- 39 Matsusue, T., & Sakaki, H. Radiative recombination coefficient of free carriers in GaAs-AlGaAs quantum wells and its dependence on temperature. *Appl. Phys. Lett.*, 50(20), 1429-1431 (1987).
- 40 Coldren, L. A., Corzine, S. W., & Mashanovitch, M. L. Diode lasers and photonic integrated circuits (Vol. 218). *John Wiley & Sons* (2012).
- 41 Seebeck, J., Nielsen, T. R., Gartner, P., & Jahnke, F. Polarons in semiconductor quantum dots and their role in the quantum kinetics of carrier relaxation. *Phys. Rev. B*, 71(12), 125327 (2005).
- 42 Moody, G., Chang, L., Steiner, T., & Bowers, J. Chip-scale nonlinear photonics for quantum light generation. *AVS Quantum Science*, 2, 041702, (2020).
- 43 Steiner, T., Castro, J., Chang, L., Dang, Q., Xie, W., Norman, J., Bowers, J., & Moody, G. Ultra-bright entangled-photon pair generation from an AlGaAs-on-insulator microring resonator. *arXiv preprint arXiv:2009.13462* (2020).
- 44 Jeremie, F., Chabran, C., & Gallion, P., Room temperature generation of amplitude squeezed light from 1550 nm distributed feedback semiconductor laser. *JOSA B*, 16(3), 460-464, (1999).
- 45 Vey, J. L., & Gallion, P., Semiclassical model of semiconductor laser noise and amplitude noise squeezing - Part II : Application to complex laser structures. *IEEE J. Quantum Electron.*, 33(11), 2105 -2110, (1997).
- 46 Qin, Z. Jing, J., Zhou, J., Liu, C., Pooser, R. C., Zhou, Z., & Zhang, W. Compact diode-laser-pumped quantum light source based on four-wave mixing in hot rubidium vapor. *Opt. Lett.*, 37, 3141-3143 (2012).